Performance Improvement of Wide-Channel Welded Plate Heat Exchanger for Bayer Precipitation Process

Qiu Ying[1], Zhang Manli[2], Wang Xinyan[3] and Zhang Limei[4]
1. R&D Engineer
2. Chief executive
3. Sales manager
4. Export Manager
Shanghai Heat Transfer Equipment, Shanghai, China
Corresponding author: by101010@163.com
https://doi.org/10.71659/icsoba2025-aa028

Abstract

In wide-channel welded plate heat exchangers, uneven flow distribution is a common issue and so a risk of scaling in the channel with smaller flow rate exists. Based on coupled CFD-DPM-Erosion numerical simulation framework, the research investigates and optimizes the erosion rate at the inlet of the second pass and the flow distribution among channels in wide-channel welded plate heat exchangers. Compared to the original design, the optimized structure demonstrates that, under varying slurry flow rates and solid concentrations, the deviation and the standard deviation of flow in the least-flow channel from the average flow is separately no more than 2.2 % and 0.94 %. Meanwhile, compared to the original design, the optimized structure demonstrates that, under varying slurry flow rates and solid concentrations, the max. erosion rate decreases by 1 to 2 orders of magnitude. This research ensures uniform flow distribution and smaller erosion rate in the second pass, laying the foundation for improving alumina production quality and extending equipment service life.

Keywords: Plate heat exchanger; Flow distribution

1. Introduction

Wide-channel welded plate heat exchangers are widely used in Bayer precipitation process due to their advantages of high heat transfer efficiency, small footprint, and compact structure. However, due to the unique characteristics of Bayer precipitation process, a large amount of aluminium hydroxide scaling adheres to the heat transfer plates, particularly in flow channels/regions with low flow velocity.

Figure 1 illustrates typical scaling deposits in the flow channels of a multi-pass heat exchanger. In wide-channel heat exchangers with multiple passes (number of passes greater than 2), the liquid-solid two-phase fluid enters the second pass via the baffle plate. Due to the reduced flow velocity near the baffle region, scaling tends to accumulate more readily in these areas. This study will (1) investigate the flow characteristics near the baffle zone in multi- pass wide-channel welded plate heat exchangers; (2) propose an optimized design to achieve uniform flow distribution; (3) evaluate the performance of this optimized design under varying solid concentrations and flow rates.

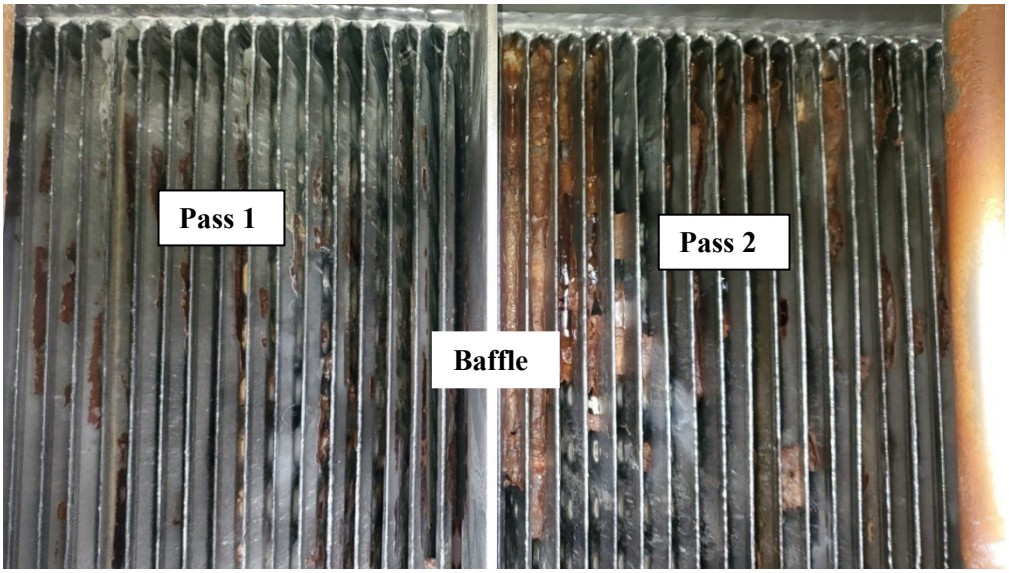

Figure 1. Scaling deposits in flow channels adjacent to the baffle plate.

2. Governing Equation

2.1 Liquid Phase Governing Equations

Within the Eulerian framework, the three-dimensional liquid-phase flow field is described by using a liquid-phase governing equation based on local averaging.

$$\frac{\partial(\rho)}{\partial t} + \nabla \cdot (\rho \boldsymbol{u}) = 0 \tag{1}$$

$$\frac{\partial(\rho \boldsymbol{u})}{\partial t} + \nabla \cdot (\rho \boldsymbol{u}\boldsymbol{u}) = -\nabla P + \nabla \cdot (\tau) - S_p + \rho \boldsymbol{g} \tag{2}$$

where:

ρ	density,
$\boldsymbol{u}$	velocity vector
$\boldsymbol{g}$	acceleration of gravity
P	pressure
$\boldsymbol{\tau}$	stress tensor
$\boldsymbol{S_p}$	liquid−solid interaction force

Based on Newton's third law, $\boldsymbol{S_p}$ in the mesh containing N particles is given by:

$$S_p = \frac{1}{V_{cell}} \sum_{i=1}^{N} F_{d,i} \tag{3}$$

where:

$\boldsymbol{F}_{d,I}$	traction force of the liquid phase acting on particle i.

The liquid-phase turbulent energy and turbulent dissipation rate in the liquid−solid two-phase flow field are described using Standard k-ε:

$$\frac{\partial(\rho_f k)}{\partial t}+\nabla\cdot(\rho_f \boldsymbol{u}_f k)=\nabla\cdot((\mu_f+\frac{\mu_{t,f}}{\sigma_k})\nabla k)+G_k-Y_k+S_k \tag{4}$$

$$\frac{\partial(\rho\varepsilon)}{\partial t}+\nabla\cdot(\rho\boldsymbol{u}\varepsilon)=\nabla\cdot((\mu+\frac{\mu_t}{\sigma_\varepsilon})\nabla\varepsilon)+G_\varepsilon-Y_\varepsilon+D_\varepsilon+S_\varepsilon \tag{5}$$

where:

k	turbulent energy
ε	turbulent dissipation rate
μ_t	turbulent viscosity
σ_k σ_ε	turbulent Prandtl numbers in the k and ε equations, which take the values of 1.0 and 1.3, respectively
G_k、G_ε	generating terms
Y_k、Y_ε	dissipation terms
D_ε	cross-diffusion term.
S_k and S_ε	source terms of the turbulent energy and turbulent dissipation rate, respectively.

2.2 Particle Phase Governing Equations

In the Lagrangian framework, particles are treated as particle packets (Parcel), each of which represents several real particles. The velocity of the dispersive particle packet is solved by Newton's second law, and its position is updated by integrating the equations of motion. The equation of motion control for a rigid, non-spherical particle packet is given by：

$$m_p\frac{d\boldsymbol{u}_p}{dt}=\frac{\pi d_p^3\rho_p}{6}[\frac{\boldsymbol{g}(\rho_p-\rho)}{\rho_p}+F_{d,p}] \tag{6}$$

where:

p	solid particle
m	mass of the particle
$\boldsymbol{g}$	acceleration of gravity
d_p	particle diameter
$\boldsymbol{F}_{d,p}$	is calculated as

$$F_{d,p}=\frac{18\mu C_D\,\mathrm{Re}_p}{24\rho_p d_p^2}(\boldsymbol{u}-\boldsymbol{u}_p) \tag{7}$$

where:

μ	liquid phase viscosity
Re_p	particle Reynolds number
C_D	drag coefficient for non-spherical particles, given as

$$C_D=\frac{24}{\mathrm{Re}_p}(1+b_1\,\mathrm{Re}_p^{b2})+\frac{b_3\,\mathrm{Re}_p}{b_4+\mathrm{Re}_p} \tag{8}$$

with:

$$b_1=\exp(2.3288-6.4581\varphi+2.4486\varphi^2) \tag{9a}$$

$$b_2=0.0964+0.5565\varphi \tag{9b}$$

$$b_3 = \exp(4.905 - 13.8944\varphi + 18.4222\varphi^2 - 10.2599\varphi^3) \quad (9c)$$

$$b_4 = \exp(1.4681 + 12.2584\varphi - 20.7322\varphi^2 + 15.8855\varphi^3) \quad (9d)$$

where:
Φ particle sphericity coefficient, calculated as

$$\varphi = \frac{s}{S} \quad (10)$$

where:
s surface area of spherical particles of the same volume as the nonspherical particles,
S surface area of non-spherical particles.

The particle turbulent dissipation characteristics are described by a random orbit model (Discrete Random Walk Model). In order to balance the numerical simulation accuracy and computational effort, the number of particle random orbitals is set to 15.

For individual solid particles, the Oka erosion model is employed to quantify the volumetric wear rate of the target wall material in a liquid-solid two-phase system with sparse particles. This model characterizes the erosive impact of low-concentration particulate flows on the heat exchanger walls. A detailed derivation and validation of the model can be found in the literature [1].

3. Simulation Method

The computational model is illustrated in Figure 2. Both the first and second passes consist of 30 flow channels, and the size of channel is 4000 mm (length) × 700 mm (width) × 12 mm (height). The liquid phase is sodium aluminate solution, while the solid phase comprises aluminium hydroxide particles. The finite volume method (FVM) was employed to discretize the governing equations of the liquid phase. The simulation utilized:

- Spatial discretization: Second-order upwind scheme
- Pressure-velocity coupling: Coupled algorithm
- Convergence criteria: Residuals < 10^{-4} for all equations

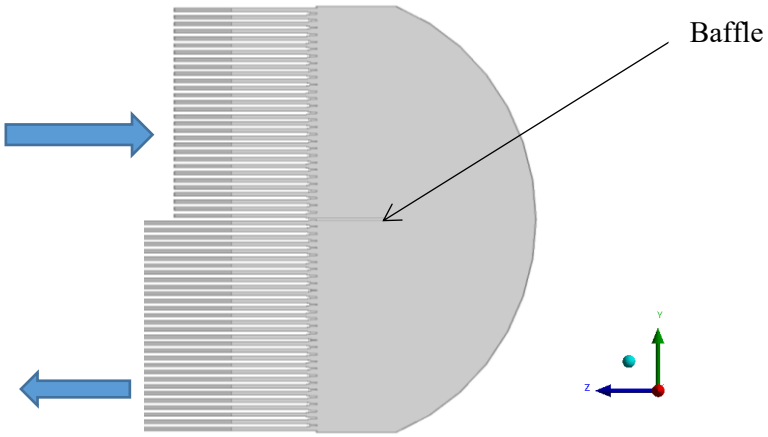

Figure 2. Model schematic diagram.

4. Results and Discussion

Under standard operating conditions, the heat exchanger operates at a flow rate Q with a solid-phase volume fraction of α. The velocity contour of the original heat exchanger under standard conditions and the flow rate distribution in each channel of the second pass are shown in Figures 3(a) and 3(b), respectively. As illustrated in Figure 3(a), when the liquid-solid two-phase fluid passes through the baffle plate and undergoes a 180° flow-direction reversal, a vortex forms, extending into the front of the second-pass channels.

This vortex leads to an uneven flow distribution:

- Channels farther from the baffle (No. 1–20) exhibit higher flow rates of the liquid-solid mixture.
- Channels closer to the baffle (No. 21–30) experience significantly reduced flow rates.

As shown in Figure 3(b), the flow rates in channels No. 26–28 are only 88 % of the average flow rate. Such low flow rates in these channels may promote scaling deposition due to insufficient shear forces.

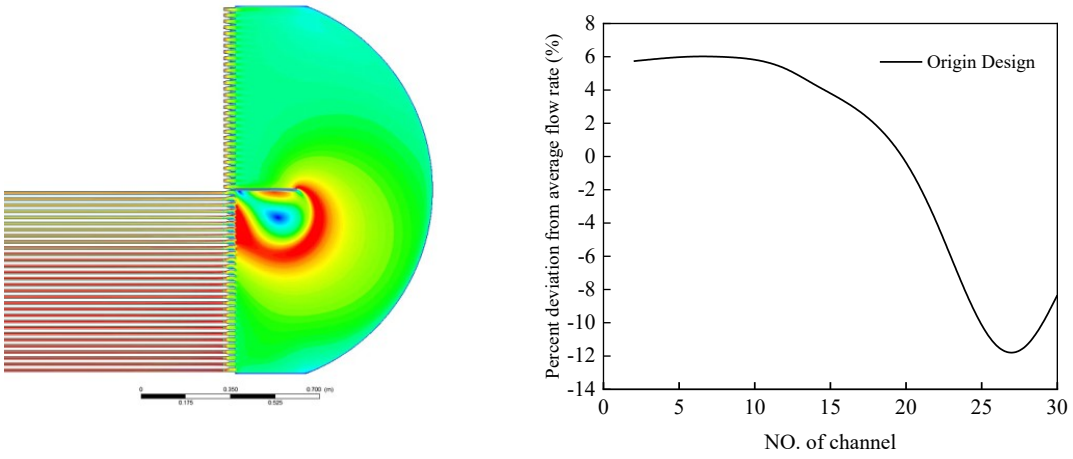

(a) (b)

Figure 3. Velocity contour and second-pass flow distribution curve in origin design.

To reduce the vortex-affected zone behind the baffle plate, two group baffle plates were installed in front of the second-pass plate bundle (Figure 5).

- Group 1 plates: Aligned parallel to the second-pass plate bundle.
- Group 2 plates: Oriented perpendicular to both Grid Plate 1 and the plate bundle.

Group 1 plates effectively shrink the vortex region downstream of the baffle (Figure 5). Subsequently, the liquid-solid mixture passes through Group 2 plates, whose resistance effect and orthogonal orientation further homogenize the flow distribution across the plate bundle's stacking direction.

As shown in Figure 6, under the standard flow rate Q and solid volume fraction α, the optimized design significantly reduces flow deviation from the average across all channels compared to the original design. Quantitative analysis reveals:

- Original design: Ratio between standard deviation of channel flow rate and average flow rate = 6.72 %
- Optimized design: Ratio between standard deviation of channel flow rate and average flow rate = 1.91 % (Shown in Table 1).

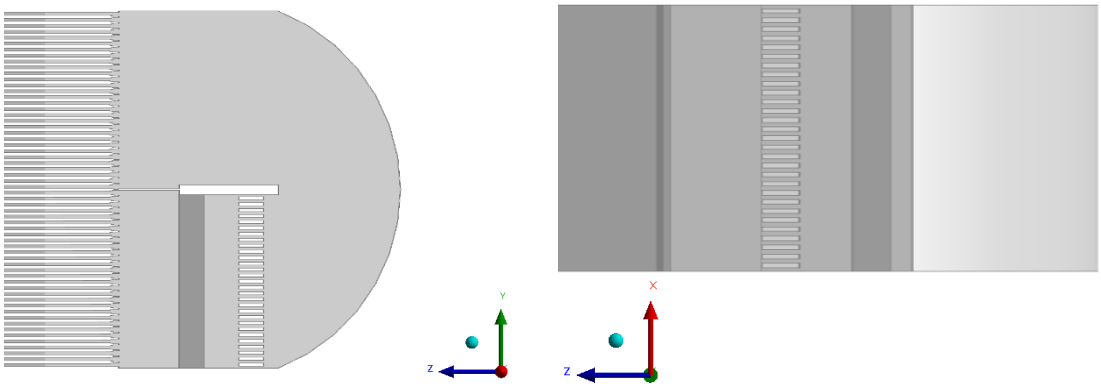

Figure 4. Optimized design for liquid-solid two-phase flow distribution.

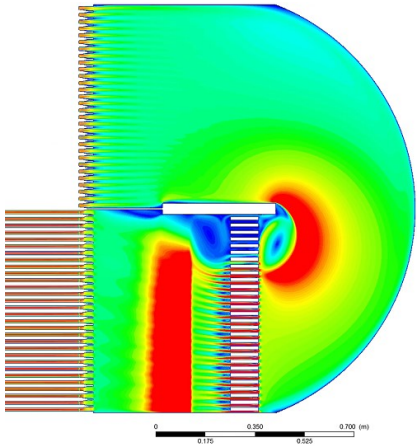

Figure 5. Velocity contour of optimized flow distribution design.

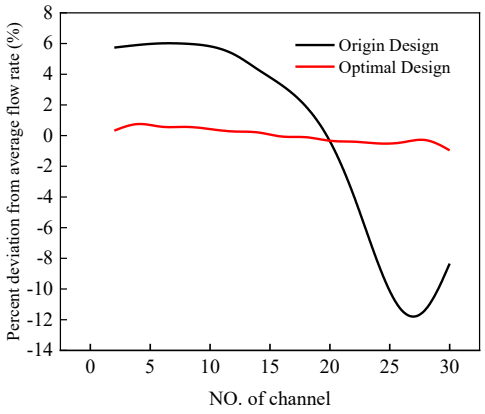

Figure 6. Percentage of channel flow rate deviation from the average.

Table 1. Ratio between standard deviation of channel flow rate and average flow rate.

(Unit: %)	Origin Design	Optimal Design
Q flow rate, α solid volume fraction	6.72	0.49

Figure 7 presents the percentage deviation of flow rates from the average under the optimized design. As depicted in Figure 7(a), after the liquid-solid two-phase fluid is redirected by the baffle plate, the inertial forces and turbulence intensity diminish with decreasing flow rates, resulting in a more uniform flow distribution among the channels. Additionally, the apparent viscosity of the liquid-solid mixture decreases with increasing solid volume fraction (α). Consequently, both the inertial forces and turbulence intensity further weaken following flow redirection at higher solid concentrations, which also promotes flow uniformity across the channels, as shown in Figure 7(b). These trends are quantitatively corroborated by the ratio between standard deviation of channel flow rate and average flow rate (see Table 2). The data demonstrates a significant reduction in flow maldistribution, validating the efficacy of the proposed design under varying flow rates and solid concentrations.

Figure 3 reveals that in the original design, large-scale vortices form at the inlet of the channels closest to the baffle plate (No. 21–30) in the second pass. Combined with the abrupt 180° flow-direction reversal, these vortices induce severe localized erosion at the front of the plate bundle in these channels, as shown in Figure 8(a).

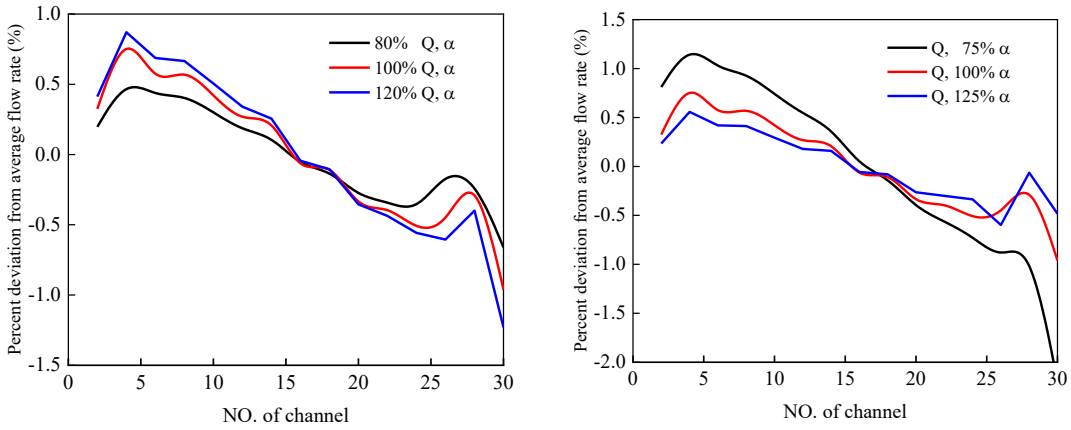

(a) (b)

Figure 7. Percentage of channel flow rate deviation from the average flow rate: (a) varying Q flow rate; (b) varying solid-phase volume fraction (Optimized design).

Table 2. Ratio between standard deviation of channel flow rate and average flow rate (optimized design).

(Unit: %)	Optimal Design
80 % Q ; α	0.34
100 % Q ; α	0.49
120 % Q ; α	0.59
Q ; 75 % α	0.94
Q ; 100 % α	0.49
Q ; 125 % α	0.35

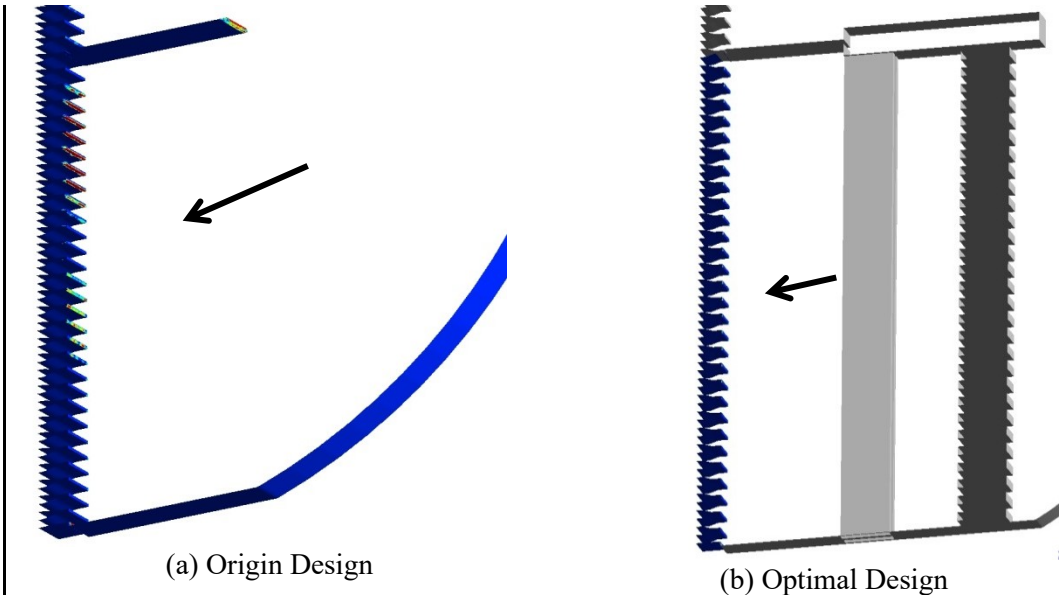

(a) Origin Design (b) Optimal Design

Figure 8. Erosion rate contour at the second-pass inlet: (a) origin design; (b) optimized design.

In contrast, Figure 5 demonstrates that the optimized design eliminates these vortices, enabling smoother entry of the liquid-solid two-phase fluid into the second-pass channels. This flow stabilization significantly reduces erosion rates at the plate bundle inlets. Quantitative comparisons confirm:

- Original design: Maximum erosion rate = 3.7×10^{-8} kg/m^2·s
- Optimized design**:** Maximum erosion rate = 3.4×10^{-9} kg/m^2·s

This represents a 90.8 % reduction in peak erosion rates.

Table 3 further compares the maximum erosion rates at the second-pass plate bundle front under varying flow rates and solid volume fraction. The optimized design achieves 1–2 orders of magnitude lower erosion rates across all tested conditions. From an erosion perspective, this improvement leads to a 10–100 extension factor of the equipment service life.

Table 3. Maximum erosion rates at the second-pass plate bundle front.

(Unit: ×10^{-9} kg/(m^{2}s))	**Origin Design**	**Optimal Design**
Max. Erosion Rate (80 % Q ; α)	24	2.4
Max. Erosion Rate (100 % Q ; α)	37	3.4
Max. Erosion Rate (120 % Q ; α)	74	4.9
Max. Erosion Rate (Q ; 75 % α)	6	0.28
Max. Erosion Rate (Q ; 100 % α)	37	3.4
Max. Erosion Rate (Q ; 125 % α)	64	4.5

5. Conclusion

Based on a coupled CFD-DPM-erosion numerical simulation framework, this study proposes a flow-uniformity-optimized design for wide-channel welded plate heat exchangers. Compared to the original design, the optimized configuration achieves:

(1) Flow Distribution Uniformity:
   - Flow deviation from the average: < 2.2% across all second-pass channels.
   - Standard deviation of flow deviations: < 1 % under varying solid concentration α and flow rate Q.

(2) Erosion Mitigation:
   - 1–2 orders of magnitude reduction in maximum erosion rates at the front ends of the second-pass plate bundle.

The proposed design ensures uniform flow distribution across all channels, effectively preventing scaling failure and front-end erosion of the plate bundle. These results establish a critical foundation for advancing the design methodology of wide-channel welded plate heat exchangers in Bayer-process alumina production.

6. Future Perspectives: Application of Thermal Imaging Technology in Scaling Diagnosis for Heat Exchangers

In wide-channel welded plate heat exchangers, excessive scaling deposits lead to performance degradation, product quality reduction, shortened equipment lifespan, energy waste, and increased carbon emissions. Therefore, monitoring of scaling conditions in such exchangers is critical for operational efficiency and sustainability.

Thermal imaging technology offers a promising solution for non-invasive scaling diagnosis. By detecting localized temperature anomalies caused by scaling blockages (e.g., foreign materials or scaling deposits), this method can identify scaling zones with high precision. Specifically, regions affected by liquid-solid two-phase scaling exhibit localized temperatures approaching those of the cooling water side due to reduced heat transfer efficiency, as illustrated in Figure 9. This thermal signature enables operators to pinpoint scaling locations and perform targeted maintenance, avoiding unnecessary full-system shutdowns.

Implementing thermal imaging-based monitoring ensures that heat exchangers operate at peak efficiency, minimizes energy losses, and extends service life by proactively addressing scaling risks. Future work should focus on integrating this technology with predictive maintenance algorithms to further optimize operational reliability in Bayer-process alumina production.

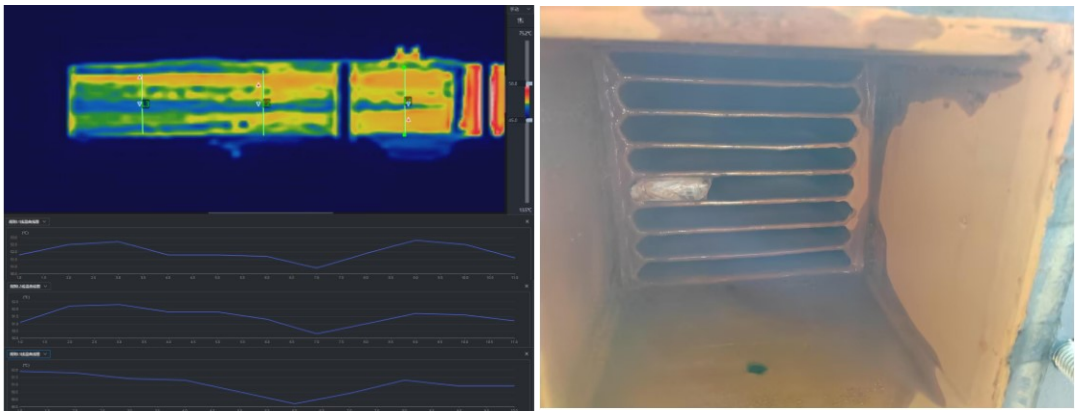

Figure 9. Experimental results of thermal imaging technology in scaling diagnosis for wide-channel welded plate heat exchangers.

7. Reference

1. Ren Libo, Long Xiangyi, Wang Xiaowei. Erosion Investigation of dimple wall using erosion-coupled dynamic mesh. *ACS Omega*, 2023,8, 39303-39314.